

## Edge detection of potential-field sources using scale-space monogenic signal: Fundamental principles

Marlon C. Hidalgo-Gato<sup>1</sup> and Valéria C. F. Barbosa<sup>2</sup>

### ABSTRACT

We have developed a new phase-based filter to enhance the edges of geologic sources from potential-field data using the local phase in the Poisson scale-space monogenic signal. The Poisson scale-space representation of a potential-field data is equivalent to performing an upward continuation of the data. We created a band-pass filter by taking the differences between two Poisson scale-space representations of the data. The local phase was defined as the arctangent of the ratio of the magnitude of the  $x$ - and  $y$ -components of the first-order Riesz transform of the filtered data to these data. These components were computed in the wavenumber domain and then transformed back into the space domain by the inverse Fourier transform. In the wavenumber domain, we found that these components are the multiplication of

the Fourier transform of the filtered data by a Fourier-domain kernel, which in turn is the multiplication of the first-order horizontal derivative filter by the first-order vertical integral filter. This operation is stable, making the local phase of the monogenic signal quite insensitive to noise. We proved that if the data were the vertical component  $f_z$  of a conservative field  $\mathbf{F}$ , the  $x$ - and  $y$ -components of the first-order Riesz transform of  $f_z$  were the horizontal components  $f_x$  and  $f_y$  of  $\mathbf{F}$ . Hence, the local amplitude of the monogenic signal of  $f_z$  is the 3D analytic signal amplitude of the scalar potential of  $\mathbf{F}$  and the local phase resembles the tilt angle (TILT). Tests on synthetic total-field anomalies and a real aeromagnetic anomaly over the Pará-Maranhão Basin, Brazil, showed that the local phase in the scale-space monogenic signal had better performance than the TILT in delineating the geologic contacts that were not seen in the original data.

### INTRODUCTION

Edge detection is an important field in image processing to enhance discontinuities in a signal. In the geophysical literature, edge-detection methods have been widely used on potential-field data. Usually, these methods are derivative- and phase-based filters that are often used to detect and delineate linear structures produced by geologic contacts and source boundaries.

The derivative-based filters have been successfully used to enhance short-wavelength anomalies produced by small and shallow sources. Examples of derivative-based filters are provided in Grauch and Cordell (1987), Roest et al. (1992), Hsu et al. (1996), Fedi and Florio (2001), Hansen and deRidder (2006), and Cooper and Cowan (2007). Among the derivative-based filters, the total-gradient filter proposed by Roest et al. (1992) is one of the most popular filters. This filter is commonly referred to as the 3D analytical signal amplitude (ASA), and is defined as the square root

of the square sum of the  $x$ ,  $y$ , and  $z$  derivatives of potential-field data  $f(x, y, z) \equiv f$ ; i.e.,

$$\text{ASA}(x, y) = \sqrt{\left(\frac{\partial f}{\partial x}\right)^2 + \left(\frac{\partial f}{\partial y}\right)^2 + \left(\frac{\partial f}{\partial z}\right)^2}. \quad (1)$$

One disadvantage of derivative-based filters is their poor performance in the presence of noise or poorer quality data. Another disadvantage is their poor performance in enhancing anomalies produced by shallow and deep bodies simultaneously.

Conversely, the phase-based filters have been usually used to enhance anomalies characterized by short- and long-wavelength spectral contents produced by shallow and deep sources. Theoretically, this is possible because the phase-based filters are grounded on a ratio of derivatives allowing the enhancement of large- and small-

Manuscript received by the Editor 14 January 2015; revised manuscript received 27 April 2015; published online 24 July 2015.

<sup>1</sup>Observatório Nacional, Rio de Janeiro, Brazil and CGG Multi-Physics, Rio de Janeiro, Brazil. E-mail: marlonchg@hotmail.com; marlon.cabrera@cgg.com.

<sup>2</sup>Observatório Nacional, Rio de Janeiro, Brazil. E-mail: valcris@on.br.

© 2015 Society of Exploration Geophysicists. All rights reserved.

amplitude anomalies equally well. Examples of phase-based filters are provided in Miller and Singh (1994), Thurston and Smith (1997), Verduzco et al. (2004), Wijns et al. (2005), Cooper and Cowan (2006), and Zhang et al. (2014). Among the phase-based filters, the tilt angle (TILT) (Miller and Singh, 1994) is the widely used edge-detection method. The TILT is defined as the arctangent of the ratio of the vertical derivative of the potential-field data to the total horizontal gradient of the field; i.e.,

$$\text{TILT}(x, y) = \tan^{-1} \left( \frac{\frac{\partial f}{\partial z}}{\sqrt{\left(\frac{\partial f}{\partial x}\right)^2 + \left(\frac{\partial f}{\partial y}\right)^2}} \right). \quad (2)$$

Theoretically, the TILT filter was introduced to cope with the difficulty of derivative-based filters in enhancing edges of shallow and deep bodies. However, in practice, low-amplitude anomalies might be missed, as shown by Santos et al. (2012). The enhancement produced by the TILT is even worse when the magnetic anomalies also have a high noise level. Hence, one challenge for edge detection in potential-field data becomes enhancing weak and noisy anomalies.

Recently, Hassan and Yalamanchili (2013) introduce the monogenic signal as a method to enhance deep sources from magnetic data. Mathematically, a complex function is defined with the 1D signal (data profile) as the real part and its Hilbert transform as the imaginary part. Similarly, the combination of a 2D signal (gridded data) and its Riesz transform is called the *monogenic signal* (Felsberg and Sommer, 2001). Hence, the combination of a 2D signal with its Riesz transform yields a generalization of the 2D analytic signal, which is named the *monogenic signal* (Dong and Kuang, 2015). Nabighian (1972) introduces the concept of the analytic signal of the magnetic data profile using the Hilbert transform, and Nabighian (1984) demonstrates the relation between the vertical and horizontal gradients of a potential-field function and their generalized Hilbert transform. Actually, the generalized Hilbert transform is the Riesz transform for 2D functions. Cooper (2014) uses the generalized Hilbert transform to calculate the zero-order analytical signal over the total magnetic intensity data.

We present a new approach for enhancing weak and noisy magnetic anomalies produced by the shallow- and deep-seated geologic contacts. Like Hassan and Yalamanchili (2013), we use the concept of the monogenic signal. In contrast with Hassan and Yalamanchili's (2013) approach, our method uses the local phase in the scale-space monogenic signal (Felsberg and Sommer, 2004), which is defined as the arctangent of the ratio of the magnitude of the  $x$ - and  $y$ -components of the first-order Riesz transform of the filtered data to these data. In the scale-space monogenic signal, the  $x$ - and  $y$ -components of the first-order Riesz transform are improved by a band-pass filter of the data. This procedure allows the enhancement of magnetic responses with different amplitudes. Tests using synthetic magnetic data and real aeromagnetic data showed that the proposed filter is potentially useful in enhancing deep and shallow geologic structures that control the basement of marginal basins.

## METHODOLOGY

### Monogenic signal

Felsberg and Sommer (2001) introduce the monogenic signal as the combination of a 2D signal (gridded data) and its first-order Riesz transform; hence, we start with a brief review of the Riesz transform.

Let  $x$  and  $y$  be real variables describing a 2D Cartesian coordinate system. The coordinate system represents the complex plane in which any point of the plane is identified by the complex number  $z \in \mathbb{C}$  with  $z = x + iy$  and  $i = \sqrt{-1}$ . Given a signal  $f(x, y) = f(z)$ , the  $n$ th-order Riesz transformation in the complex plane is defined by Felsberg and Sommer (2001) as

$$\begin{aligned} R^n \{f(z)\} &= R\{R\{\dots R\{f(z)\}\}\} \\ &= -\frac{n}{2\pi} \int_{\tau \in \mathbb{C}} \frac{f(\tau)}{(z - \tau)^n \|z - \tau\|^{2-n}} d\tau, \end{aligned} \quad (3)$$

where  $\tau \in \mathbb{C}$  with  $\tau = \tau_x + i\tau_y$ .

The first-order Riesz transform in the complex plane is given by

$$\begin{aligned} R^1 \{f(z)\} &= -\frac{1}{2\pi} \int_{\tau} \frac{(x - \tau_x)}{\|z - \tau\|^3} f(\tau) d\tau \\ &\quad + i \frac{1}{2\pi} \int_{\tau} \frac{(y - \tau_y)}{\|z - \tau\|^3} f(\tau) d\tau, \end{aligned} \quad (4)$$

which can be rewritten as

$$R^1 \{f(z)\} = -r_x \{f(z)\} + ir_y \{f(z)\}, \quad (5)$$

where  $r_x$  and  $r_y$  are, respectively, the  $x$ - and  $y$ -components of the first-order Riesz transform of  $f(x, y)$  defined by

$$r_x(f) = \frac{x}{2\pi(x^2 + y^2)^{\frac{3}{2}}} * f(x, y), \quad (6a)$$

and

$$r_y(f) = \frac{y}{2\pi(x^2 + y^2)^{\frac{3}{2}}} * f(x, y), \quad (6b)$$

where the asterisk (\*) represents convolution.

The monogenic signal is defined as a 3D vector given by

$$\mathbf{m} = \begin{bmatrix} f \\ r_x \\ r_y \end{bmatrix}, \quad (7)$$

where the component  $f \equiv f(x, y)$  represents the even part of the signal and the components  $r_x$  and  $r_y$  (equations 6a and 6b) represent the odd part of the signal. Let us consider a 3D coordinate system defined by the components of the monogenic signal ( $f$ ,  $r_x$ , and  $r_y$ ) as shown in Figure 1. Using this 3D vector representation of the monogenic signal (Figure 1), we can define:

1) the local amplitude of the monogenic signal given by

$$A(x, y) = \sqrt{r_x^2 + r_y^2 + f^2}, \quad (8)$$

2) the local orientation of the monogenic signal given by

$$\theta(x, y) = \tan^{-1} \left( \frac{r_y}{r_x} \right), \quad (9)$$

3) the local phase of the monogenic signal given by

$$\varphi(x, y) = \tan^{-1} \left( \frac{\sqrt{r_x^2 + r_y^2}}{f} \right). \quad (10)$$

**The Riesz transform in the wavenumber domain**

Let us assume that the functions  $f(x, y)$ ,  $r_x$  (equation 6a) and  $r_y$  (equation 6b) have Fourier transforms given by  $F$ ,  $R_x$ , and  $R_y$ , respectively. Taking the Fourier-convolution theorem — which states that the convolution in the space domain transforms to a multiplication in the wavenumber domain — and using the Fourier transformations

$$\mathcal{F} \left\{ \frac{x}{2\pi(x^2 + y^2)^{\frac{3}{2}}} \right\} = i \frac{u}{\sqrt{u^2 + v^2}} \quad (11)$$

and

$$\mathcal{F} \left\{ \frac{y}{2\pi(x^2 + y^2)^{\frac{3}{2}}} \right\} = i \frac{v}{\sqrt{u^2 + v^2}}, \quad (12)$$

the  $x$ - and  $y$ -components of the first-order Riesz transform (equations 6a and 6b) can be easily computed, in the wavenumber domain, as

$$R_x(u, v) = i \frac{u}{\sqrt{u^2 + v^2}} F, \quad (13a)$$

and

$$R_y(u, v) = i \frac{v}{\sqrt{u^2 + v^2}} F, \quad (13b)$$

where  $u$  and  $v$  are inversely related to wavelengths in the  $x$ - and  $y$ -directions, respectively.

**Scale-space monogenic signal**

The scale-space technique handles image structures at different scales by representing a signal as a one-scale-parameter family without changing the sizes of the structures. By assuming a non-negative scale parameter  $h$ , Felsberg and Sommer (2004) define the Poisson space-scale representation  $f_p(x, y, h)$  as the convolution of the signal  $f(x, y)$  with the Poisson kernel distribution; i.e.,

$$f_p(x, y, h) = \frac{h}{2\pi(h^2 + x^2 + y^2)^{\frac{3}{2}}} * f(x, y). \quad (14a)$$

In the wavenumber domain, the Poisson scale-space representation of the signal  $f(x, y)$  is given by

$$F_p \equiv \mathcal{F}\{f_p\} = e^{-2\pi h \sqrt{u^2 + v^2}} F, \quad (14b)$$

which is exactly equal to the upward continuation of the potential-field data at the continuation height  $h$ .

The scale parameter  $h$  controls the degree of resolution applied to the signal. For example, if  $h$  tends to zero, the scale-space repre-

sentation  $f_p(x, y, h)$  of the signal  $f(x, y)$  is the signal itself. The larger the value of  $h$  the lesser the details of the structures without changing the dimensions of the data. This means that an increase in  $h$  leads to a decrease in the resolution of the scale-space representation  $f_p(x, y, h)$  of the signal  $f(x, y)$ .

To enhance low- and high-wavenumber features, Felsberg and Sommer (2004) propose a band-pass filter using a combination of coarse  $h_c$  and fine  $h_f$  Poisson-scale parameters with  $h_c > h_f > 0$ . In the wavenumber domain, this can be performed by the difference between two Poisson scale-space representations of the signal  $f(x, y)$  using the two Poisson-scale parameters  $h_c$  and  $h_f$ ; i.e.,

$$F_{bp} = \left( e^{-2\pi h_f \sqrt{u^2 + v^2}} - e^{-2\pi h_c \sqrt{u^2 + v^2}} \right) F. \quad (15)$$

Equation 15 is the Poisson scale-space representation of the signal  $f(x, y)$  filtered by a band-pass filter, which is accomplished by the difference between the upward continuations of the signal at two elevations of  $h_f$  and  $h_c$ . Hence, the unit of  $h_f$  and  $h_c$  will be the same as the data grid unit.

Like the monogenic signal (equation 7), the Poisson scale-space monogenic signal of  $f(x, y)$  filtered by a band-pass filter is a 3D vector defined, in the wavenumber domain, as

$$\mathbf{m}_p = \begin{bmatrix} F_{bp} \\ R_{xp} \\ R_{yp} \end{bmatrix}, \quad (16)$$

where  $F_{bp}$  is given by equation 15 and  $R_{xp}$  and  $R_{yp}$  are, respectively, the  $x$ - and  $y$ -components of the first-order Riesz transform of  $F_{bp}$  expressed by

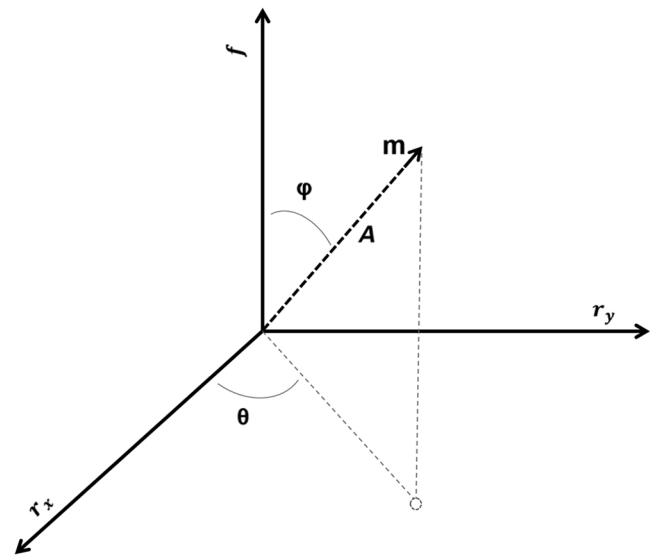


Figure 1. Schematic representation of monogenic signal vector  $\mathbf{m}$  (equation 7) in 3D Euclidean space. The component  $f \equiv f(x, y)$  is the signal, and the components  $r_x$  and  $r_y$  are the  $x$ - and  $y$ -components of the first-order Riesz transform of the signal. The local amplitude, local orientation, and local phase of the monogenic signal are  $A(x, y)$ ,  $\theta(x, y)$ , and  $\varphi(x, y)$ , respectively.

$$R_{xp}(u, v) = i \frac{u}{\sqrt{u^2 + v^2}} F_{bp}, \quad (17a)$$

and

$$R_{yp}(u, v) = i \frac{v}{\sqrt{u^2 + v^2}} F_{bp}. \quad (17b)$$

In terms of computational details, the local amplitude and the local phase in the Poisson scale-space monogenic signal of  $f(x, y)$  filtered by a band pass are computed in two steps. In the first step, we compute the elements of the vector  $\mathbf{m}_p$  (equation 16) using equations 15, 17a, and 17b. Because these components are computed in the wavenumber domain, the second step consists in transforming the elements of  $\mathbf{m}_p$  back into the space domain by the inverse Fourier transform. Finally, we calculate the local amplitude and local phase. These procedures are extremely rapid, allowing an efficient interpretation of the edges of geologic sources from large data sets.

## FUNDAMENTAL RELATIONS

### Relations between the Riesz transform and the potential-field components

Considering a potential field  $U(x, y, z) \equiv U$  in Cartesian coordinates, which satisfies the Laplace's equation  $\nabla^2 U = 0$  at places free

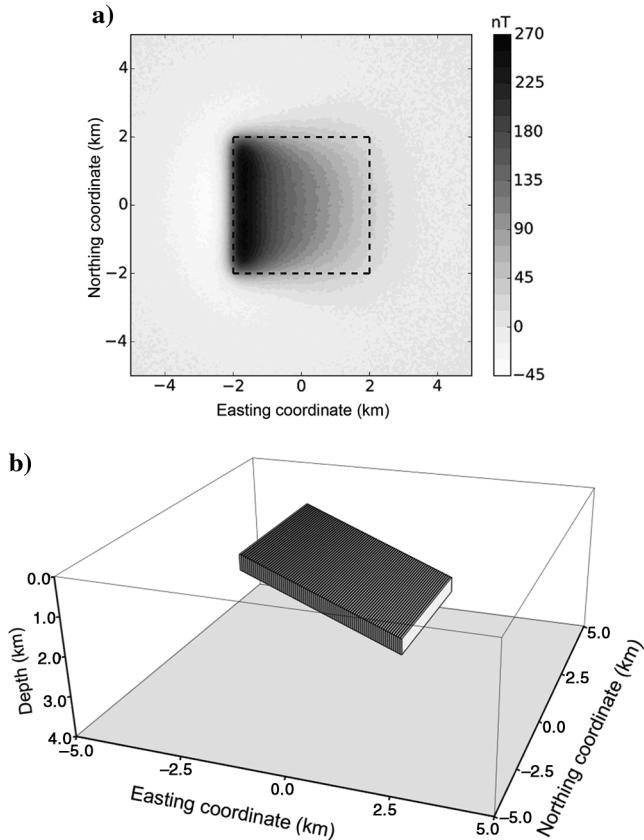


Figure 2. Synthetic test. (a) Noise-corrupted total-field anomaly produced by (b) the isolated dipping intrusion. The dashed black lines in panel (a) indicate the horizontal projections of the edges of the dipping source.

of all sources, the 3D conservative force field  $\mathbf{F}$  is related to its potential field  $U$  according to  $\mathbf{F} = \nabla U$ . The three Cartesian components of the force field in three orthogonal directions are

$$\mathbf{F} \equiv \begin{bmatrix} f_x \\ f_y \\ f_z \end{bmatrix} = \begin{bmatrix} \frac{\partial U}{\partial x} \\ \frac{\partial U}{\partial y} \\ \frac{\partial U}{\partial z} \end{bmatrix}. \quad (18)$$

In the wavenumber domain, the horizontal and vertical components of the force field  $\mathbf{F}$  are given by

$$\begin{aligned} \mathcal{F}\{f_x\} &\equiv \mathcal{F}\left\{\frac{\partial U}{\partial x}\right\} = iu\mathcal{F}\{U\} \\ \mathcal{F}\{f_y\} &\equiv \mathcal{F}\left\{\frac{\partial U}{\partial y}\right\} = iv\mathcal{F}\{U\} \end{aligned} \quad (19)$$

and

$$\mathcal{F}\{f_z\} \equiv \mathcal{F}\left\{\frac{\partial U}{\partial z}\right\} = \sqrt{u^2 + v^2}\mathcal{F}\{U\}. \quad (20)$$

Hence, given the vertical component  $f_z = \partial U/\partial z$  of the force field, the  $x$ - and  $y$ -components of the first-order Riesz transform of  $f_z$  in the wavenumber domain (equations 13a and 13b) can be expressed by

$$R_x = i \frac{u}{\sqrt{u^2 + v^2}} \mathcal{F}\left(\frac{\partial U}{\partial z}\right) = iu\mathcal{F}\{U\}, \quad (21a)$$

and

$$R_y = i \frac{v}{\sqrt{u^2 + v^2}} \mathcal{F}\left(\frac{\partial U}{\partial z}\right) = iv\mathcal{F}\{U\}. \quad (21b)$$

The reader will recognize that, in the wavenumber domain, the  $x$ - and  $y$ -components of the first-order Riesz transform (equations 21a and 21b) of the vertical component  $f_z$  are the Fourier transforms of the horizontal components  $f_x$  and  $f_y$  of a conservative force field  $\mathbf{F}$ ; i.e.,

$$R_x = \mathcal{F}(f_x), \quad (22a)$$

and

$$R_y = \mathcal{F}(f_y). \quad (22b)$$

Hence, in the space domain, the  $x$ - and  $y$ -components of the first-order Riesz transform (equations 22a and 22b) of the vertical component  $f_z$  are the horizontal components of a conservative force field; i.e.,

$$r_x(f_z) = f_x, \quad (23a)$$

and

$$r_y(f_z) = f_y. \quad (23b)$$

**Local amplitude and local phase of the monogenic signal versus the analytic signal and tilt angle**

Using equations 23a and 23b, one can easily prove the relationships between the monogenic signal and the 3D analytic signal and TILT.

Specifically, the local amplitude of the monogenic signal (equation 8) of the vertical component  $f_z$  of a conservative force field can be written as

$$A(x, y) = \sqrt{f_x^2 + f_y^2 + f_z^2}. \quad (24)$$

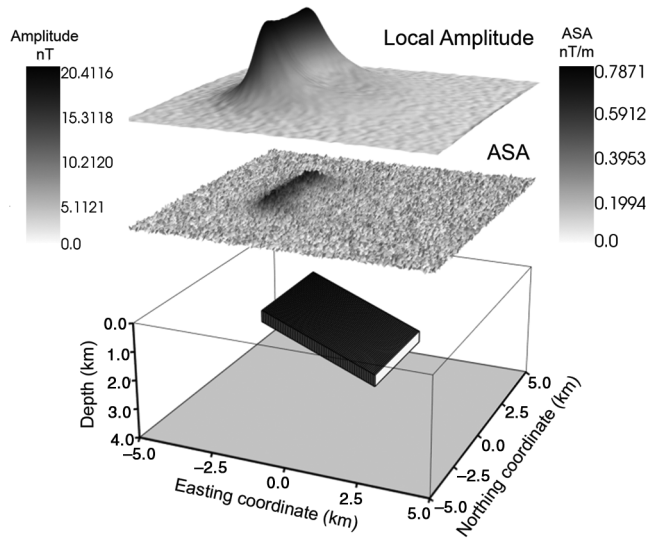


Figure 3. Perspective view of the simulated dipping intrusion and the enhancements of the total-field anomaly of Figure 2a using the ASA and the local amplitude in the scale-space monogenic signal.

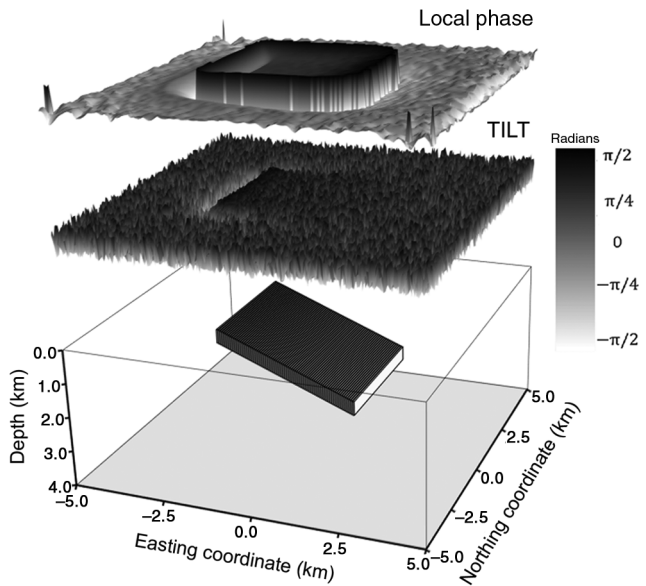


Figure 4. Perspective view of the simulated dipping intrusion and the enhancements of the total-field anomaly of Figure 2a using the TILT and the local phase in the scale-space monogenic signal.

Notice that equation 24 is the 3D analytic signal amplitude of the scalar potential  $U(x, y, z) \equiv U$  of a conservative force field  $\mathbf{F}$ ; i.e.,

$$ASA(x, y) = \sqrt{\left(\frac{\partial U}{\partial x}\right)^2 + \left(\frac{\partial U}{\partial y}\right)^2 + \left(\frac{\partial U}{\partial z}\right)^2}. \quad (25)$$

However, this is not what is known as the 3D analytic signal amplitude (Roest et al., 1992), mentioned by Nabighian et al. (2005).

Equations 23a and 23b show that the local phase of the monogenic signal (equation 10) of the vertical component  $f_z$  of a conservative force field can be written as

$$\varphi(x, y) = \tan^{-1}\left(\frac{\sqrt{f_x^2 + f_y^2}}{f_z}\right). \quad (26)$$

Notice that equation 26 resembles the TILT (Miller and Singh, 1994). Like TILT, the local phase has a value between  $-90^\circ$  and  $+90^\circ$ . In contrast, the zero contour of the TILT delineates the geologic contacts, whereas maximum contour of the local phase delineates the geologic contacts.

**Why are local amplitude and local phase of the monogenic signal better than the analytic signal amplitude and TILT?**

Note that, in the wavenumber domain, the components  $R_x$  and  $R_y$  of the monogenic signal of the data (equations 13a and 13b) and the components  $R_{xp}$  and  $R_{yp}$  of the Poisson scale-space monogenic signal of the filtered data (equations 17a and 17b) use the first-order horizontal derivative filters ( $iu$  and  $iv$ ) and the first-order vertical

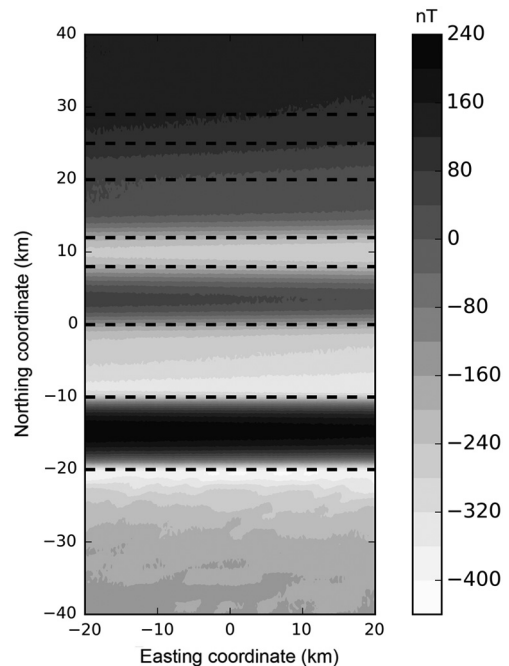


Figure 5. Synthetic test. Noise-corrupted total-field anomaly produced by the simulated 3D extensional basin (Figure 6). The dashed black lines indicate the horizontal projections of the eight geologic contacts pinpointed in Figure 6 as labels 1–8.

integral filter ( $1/\sqrt{u^2 + v^2}$ ). Although the horizontal derivative filters enhance the high-wavenumber components of a signal, the vertical integral filter counteracts this enhancement by attenuating the high-wavenumber spectral content. The balance between the amplification and attenuation of the high-wavenumber components makes the local amplitude (equation 8) and the local phase (equation 10) of the monogenic signal weakly sensitive to noise. In contrast, the 3D analytic signal amplitude (Roest et al., 1992) and the TILT (Miller and Singh, 1994) require the horizontal and vertical derivatives of the signal that amplify the high-wavenumber components of the anomalies. Hence, the 3D analytic signal amplitude and the TILT are more sensitive to the presence of noise in the signal.

### APPLICATION TO SYNTHETIC DATA

We present two tests using synthetic noise-corrupted total-field anomalies. In the first one, we simulate an isolated dipping intrusion with a shallow top and deep bottom. In the second test, we simulate a passive margin basin in which crustal stretching leads to the development of a complex system of normal faults resulting in a series of basement horsts and grabens.

#### Isolated dipping intrusion

Figure 2a shows, in grayscale, the simulated noise-corrupted total-field anomaly produced by a magnetized deep-bottomed dipping

Figure 6. Synthetic test. Perspective view of the simulated 3D extensional basin such as the one formed during the Atlantic rifting process. The labels 1–8 locate the eight geologic contacts between the basement and the sediment. The upper surface represents the bathymetry.

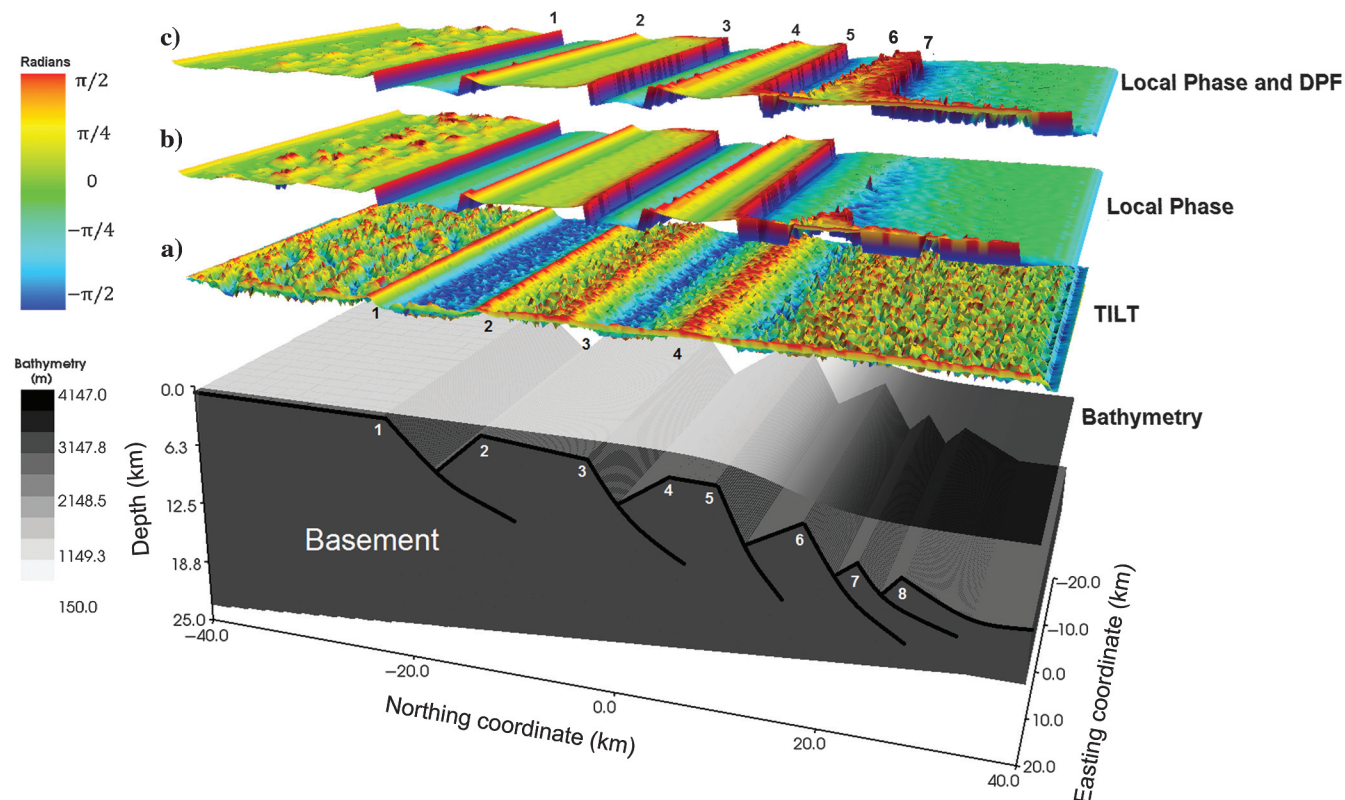
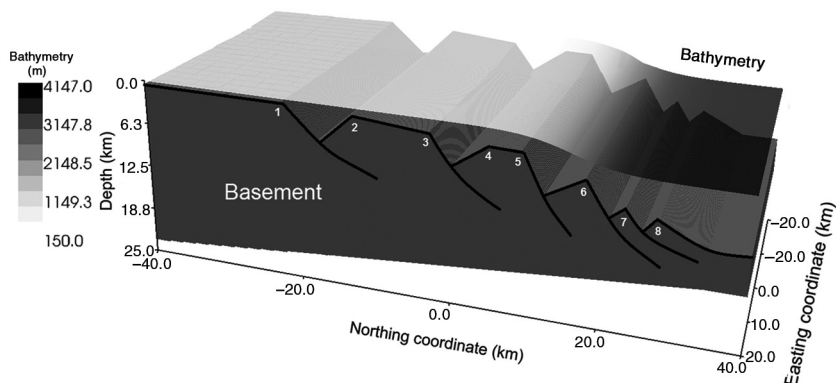


Figure 7. Synthetic test. Perspective view of the simulated 3D extensional basin and the enhancements of the total-field anomaly of Figure 5 using (a) the TILT, (b) the local phase in the scale-space monogenic signal, and (c) the local phase in the scale-space monogenic signal in cascade with the DPF. The total-field anomaly enhanced by the DPF is not shown. The labels 1–8 locate the eight geologic contacts between the basement and the sediments.

body (Figure 2b) enclosed in a nonmagnetic medium. The body has induced magnetization only with an inclination of  $90^\circ$ , a declination of  $0^\circ$ , and an intensity of 2 A/m. The depths to the top and bottom of the simulated body are 0.2 m and 2.7 km, respectively. The horizontal projections of the edges of the body are shown in Figure 2a as the dashed lines superimposed on the anomaly. Using Uieda et al. (2013), we calculate the total-field anomaly at a 150-m height on a regular grid of  $200 \times 200$  observation points in the north–south and east–west directions with grid spacing of 50 m along both directions. The anomaly was corrupted with pseudorandom zero-mean Gaussian noise with a standard deviation of 10 nT. This example illustrates the eastward anomaly attenuation caused by the eastward increase of the distance between the source and magnetometer. We can note that the horizontal projection of the shallowest edge of the body can be easily delimited by the magnetic response (Figure 2a); however, the response becomes weak over the deepest edge of the body, and its horizontal projection cannot be inferred easily from inspecting the anomaly.

We enhance the original signal (Figure 2a) to delimit the horizontal projections of the edges of the simulated dipping body (Figure 2b). The enhancements produced on the original data by applying the ASA and TILT are, respectively, shown in Figures 3 and 4 (lower filtered outputs). We note that neither ASA nor TILT enhances all the edges of the body. These filtered outputs are virtually similar to the total-field anomaly (Figure 2a) with the disadvantage of a strong amplification of the noise.

However, the local amplitude in the scale-space monogenic signal (upper filtered output in Figure 3) with  $h_c = 0.2$  km and  $h_f = 0.15$  km does not amplify the noise. However, it shows a strong correlation with ASA, and thus, it does not enhance the deepest edge of the body. In contrast, the local phase in the scale-space monogenic signal (upper filtered output in Figure 4) enhances all the edges of the simulated dipping body without amplifying the noise. We can note that the maximum value of the local phase in the space-scale monogenic signal shows a close agreement with the horizontal projections of the edges of the dipping bodies.

### Passive marginal basin

In this test, we compute a noise-corrupted total-field anomaly (Figure 5 in grayscale) produced by a simulated 3D extensional basin (Figure 6) such as the one found in an offshore Brazilian passive margin. The tectonic framework of the basement relief of this basin is characterized by a series of horsts and grabens. This framework defines eight geologic contacts between the basement and the sediment, which are labeled 1–8 in Figure 6. This simulated structural framework is strongly controlled by normal faults such as the ones implanted during the South Atlantic rifting process.

The magnetic basement is uniformly magnetized by induction only with a magnetization intensity of 2 A/m, an inclination of  $-2^\circ$ , and a declination of  $-20^\circ$ . The geometry of the rift was extrapolated to the east and west directions to simulate 2D geologic structures. Using Uieda et al. (2013), we calculate the total-field anomaly at 150-m height on a regular grid of  $400 \times 200$  observation points in the north–south and east–west directions with a grid spacing of 200 m along both directions. The anomaly was corrupted with pseudorandom zero-mean Gaussian noise with a standard deviation of 10 nT.

We apply the TILT to the total-field anomaly of Figure 5. Figure 7a shows that the TILT enhances four of the eight geologic con-

tacts clearly. However, the local phase in the scale-space monogenic signal with  $h_c = 0.4$  km and  $h_f = 0.2$  km (Figure 7b) applied to the same anomaly clearly delimits five of the eight geologic contacts. Only the three deepest geologic contacts were not enhanced.

We explore the assumption of complementarity by applying the local phase in the scale-space monogenic signal to the total-field anomaly enhanced by the deep-pass filter (DPF; Santos et al., 2012). First, we apply the DPF to the total-field anomaly (Figure 5), and next, we apply the scale-space monogenic phase to the DPF output (not shown). Figure 7c shows the application of the DPF in combination with the local phase in the monogenic scale space with  $h_c = 0.4$  km and  $h_f = 0.2$  km. We note that this filtered output discloses geologic contacts that were not revealed in individual applications of the filters. Figure 7c enhances seven of eight geologic contacts. Only the deepest geologic contact was not delimited.

In this test, the data were not reduced to the pole because we are interpreting 2D geologic contacts. However, we stress that the local amplitude and local phase in the monogenic scale-space are filters that depend on everything that the magnetic field itself may depend.

### ANALYSIS OF THE LOCAL PHASE IN THE SCALE-SPACE MONOGENIC SIGNAL

To understand the role of the band-pass filter in the local phase in the Poisson scale-space monogenic signal, we simulate a synthetic test produced by two magnetized prisms (Figure 8) by induction

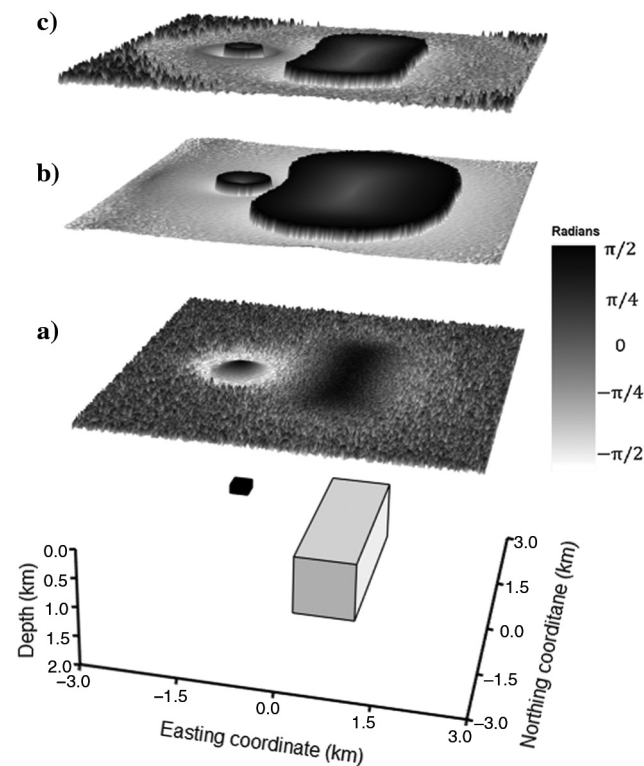


Figure 8. Synthetic test. Perspective view of the simulated shallow and deep prisms magnetized by induction only in the vertical direction. The enhancements produced by (a) TILT, (b) local phase in the scale-space monogenic signal using the Poisson representation of the data (equation 14b) with  $h = 0.2$  km, and (c) local phase in the scale-space monogenic signal with a band-pass filtered data (equation 15) setting  $h_c = 0.3$  km and  $h_f = 0.2$  km.

only with a constant magnetization with an inclination of  $90^\circ$  and intensities of 1 A/m (shallow prism) and 0.1 A/m (deep prism). We calculate the noise-corrupted total-field anomaly at 150-m height on a regular grid of  $200 \times 200$  observation points in the north–south and east–west directions. The anomaly (not shown) was corrupted with a pseudorandom zero-mean Gaussian noise with a standard deviation of 0.25 nT. We apply three different types of filters to the noise-corrupted total-field anomaly: (1) the TILT (Figure 8a), (2) the local phase in the scale-space monogenic signal

using the Poisson representation of the data (equation 14b) with  $h = 0.2$  km (Figure 8b), and (3) the local phase in the scale-space monogenic signal with a band-pass filtered data (equation 15) setting  $h_c = 0.3$  km and  $h_f = 0.2$  km (Figure 8c). The local phase in the monogenic signal with the Poisson scale-space representation of the data (equation 14b) reduces the resolution of the data and generates features that appear to be from larger bodies (Figure 8b). Conversely, the local phase in the monogenic signal with the band-pass-filtered data (equation 15) generates smaller features for the

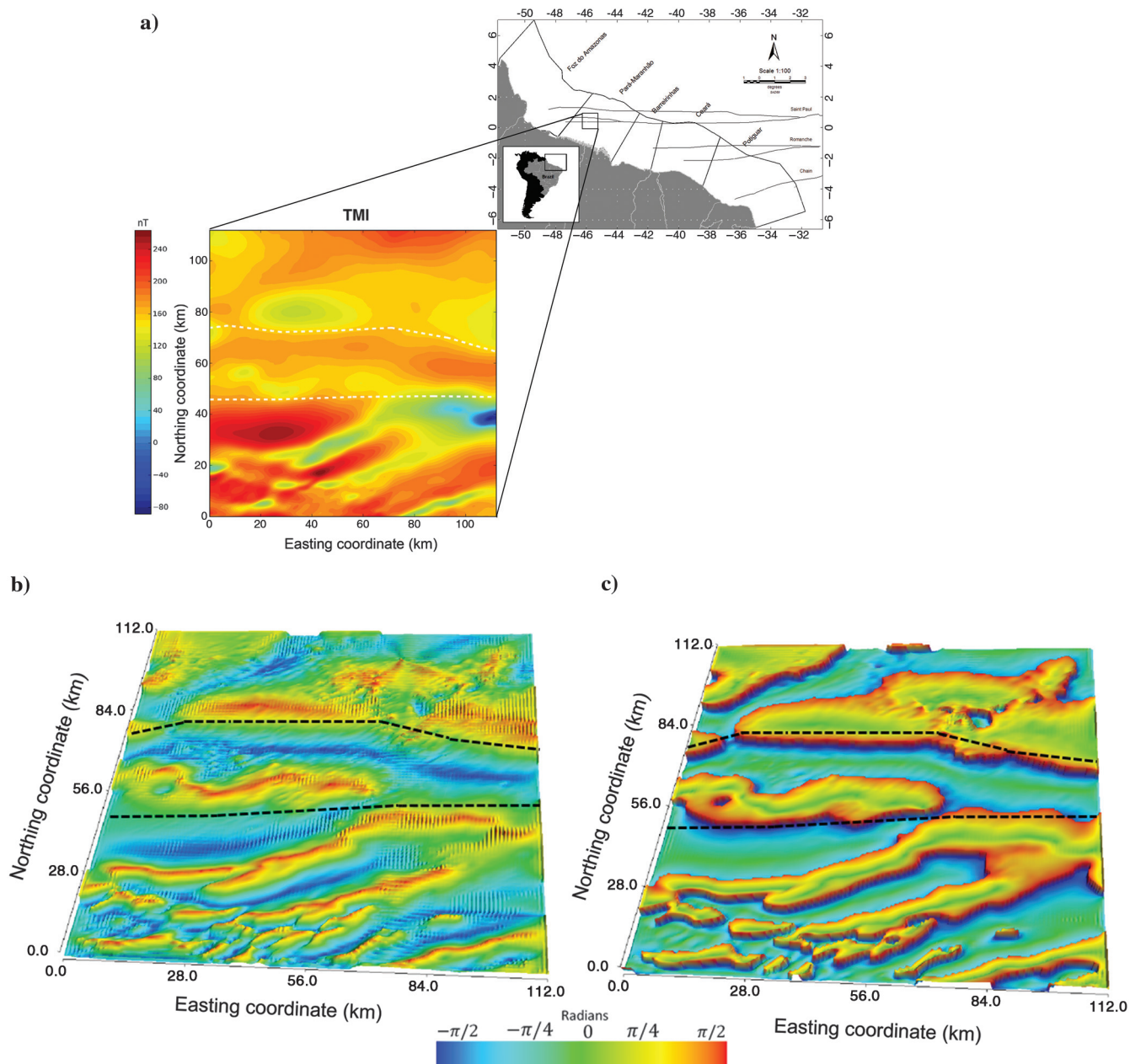


Figure 9. Real test. (a) Aeromagnetic total-field anomaly over Pará-Maranhão Basin, Brazil. The dashed white lines indicate the horizontal projections of the east–west edges of the Saint Paul Fracture Zone. The inset shows the continental margin of the northeastern Brazil with the Saint Paul, Romanche and Chain Fracture Zones (in gray lines) and the sedimentary basins (polygons in black lines). The study area is outlined with a square within the Pará-Maranhão Basin. The enhancements of the total-field anomaly using (b) the TILT and (c) the local phase in the scale-space monogenic signal. The dashed black lines in panels (b and c) are correlated with the Saint Paul Fracture Zone shown in panel (a), which cuts across the continental margin into the Pará-Maranhão Basin.

shallow and deep bodies (Figure 8c). The scale-space parameters ( $h_c$  and  $h_f$ ), expressed in units of the grid spacing, are chosen based on the spectral content of the data.

### APPLICATION TO REAL DATA

We have applied our method to a total-field anomaly from a study area located in the northwest of the Pará-Maranhão Basin in the Brazilian equatorial margin. The Brazilian equatorial margin encompasses a family of the northwest–southeast-trending en-echelon basins including the Pará-Maranhão Basin. The Pará-Maranhão Basin is located entirely offshore on Brazil's northern coast (inset of Figure 9a), between approximately 2°S and 2°N, and 48°W and 42°W. The Barreirinhas and Foz do Amazonas Basins define its southeast and northwest limits, respectively. The tectonic evolution of Pará-Maranhão Basin is linked to the Gondwana breakup and the opening of the Equatorial Atlantic Ocean. The rifting process was established mostly over the Archean São Luis Craton, which is a fragment of the West African Craton. The Pará-Maranhão Basin is a typical continental transform margin dominated either by oblique extension or by pure shear movements in a dextral sense. The northwest portion of the Pará-Maranhão Basin, where the study area is located, is affected by the Saint Paul Fracture Zone which is a strong system of east–west-trending faults and fractures (Zalán, 2011).

The magnetic data (Figure 9a) consist of a high-resolution aeromagnetic survey over the Brazilian equatorial margin. The flight lines were flown at a height of 150 m, with line spacing of 500 m and 1 km over, respectively, the shallow water in the continental shelf and the deep water in the continental slope. The data set used herein corresponds to a regular grid of  $225 \times 225$  observation points in the north–south and east–west directions with a grid spacing of 500 m along both directions. The geomagnetic field has an inclination of  $-1.9^\circ$  and declination of  $-20.3^\circ$ .

Figure 9b and 9c shows the results of filtering the total-field anomaly (Figure 9a), respectively, with the TILT and the local phase in the scale-space monogenic signal using a  $h_c = 0.5$  km and  $h_f = 0.4$  km. We note that the original total-field anomaly (Figure 9a) and the enhanced outputs (Figure 9b and 9c) show striking differences. However, as we show with synthetic data, the enhanced geologic contacts (or lineaments) produced by the TILT (Figure 9b) are blurred, whereas the local phase in the monogenic scale space (Figure 9c) displays geologic features that are not clearly apparent in the TILT image.

The local phase in the monogenic scale space (Figure 9c) highlights clearly two patterns of lineaments and geologic contacts. In the northern and central portions of the study area, the east–west lineaments dominate. We interpret the main east–west lineament (dashed lines in Figure 9c) as magnetic expressions of the Saint Paul Fracture Zone cutting the continental margin into the Pará-Maranhão Basin (inset of Figure 9a). Conversely, in the southern portion of the study area, the local phase in the monogenic scale space reveals the predominance of the northeast–southwest lineaments. These lineaments are located over the shallow basement of Pará-Maranhão Basin and they could be related to a late amalgamation of different terrains that composed the São Luis Craton. Notice that the east–west and northeast–southwest lineaments are revealed more subtly in the TILT map (Figure 9b).

### CONCLUSIONS

We have proposed the local phase in the monogenic scale space as a new edge-detection filter to enhance aeromagnetic data. Our filter computes, in the wavenumber domain, the  $x$ - and  $y$ -components of the first-order Riesz transform of the band-pass filtered data. Then, these components and the filtered data are transformed back into the space domain by the inverse Fourier transform. Finally, the local phase in the monogenic scale space is computed as the arctangent of the ratio of the magnitude of the  $x$ - and  $y$ -components of the first-order Riesz transform of the filtered data to these data. The band-pass filter is created using the Poisson scale-space representation of the data. The TILT and the local phase are able to enhance strong and weak anomalies. Besides, the local phase in the monogenic scale space has the advantage of being weakly sensitive to random noise. The results from a synthetic example and aeromagnetic data from Pará-Maranhão Basin in offshore Brazilian passive margin showed that the local phase in the monogenic scale space is effective in enhancing lineaments that are neither directly inferred from inspection of the magnetic anomaly nor easily revealed by other filters such as the TILT. Different practical applications of the local phase in the monogenic scale space are feasible to interpret other geologic environments with similar challenges of enhancing the magnetic responses of deep and shallow sources. The application of this approach to enhance gravity, multiple-component gravity gradiometry, and magnetic gradient data has no methodological obstacles.

### ACKNOWLEDGMENTS

The authors are grateful to the assistant editor V. Socco, the associate editor R. Smith, S. Goussev, H. Zhang, U. K. Singh, and anonymous reviewers for their questions and suggestions. We thank CGG Multi-Physics for the permission to use the field data. M. C. Hidalgo-Gato was supported by the Research and Development project of CGG Multi-Physics Brazil and Sinochem Petróleo Brasil Ltda in the Brazilian equatorial margin. V. C. F. Barbosa was supported in this research by a fellowship from Conselho Nacional de Desenvolvimento Científico e Tecnológico (CNPq), Brazil. Additional support for V. C. F. Barbosa is provided by the Brazilian research agency FAPERJ (grant E-26/103.175/2011). We acknowledge the open-source Python toolkit for geophysical modeling and inversion called *Fatiando a Terra* (Portuguese for slicing the earth).

### REFERENCES

- Cooper, G. R. J., 2014, Reducing the dependence of the analytic signal amplitude of aeromagnetic data on the source vector direction: *Geophysics*, **79**, no. 4, J55–J60, doi: [10.1190/geo2013-0319.1](https://doi.org/10.1190/geo2013-0319.1).
- Cooper, G. R. J., and D. R. Cowan, 2006, Enhancing potential field data using filters based on the local phase: *Computers and Geosciences*, **32**, 1585–1591, doi: [10.1016/j.cageo.2006.02.016](https://doi.org/10.1016/j.cageo.2006.02.016).
- Cooper, G. R. J., and D. R. Cowan, 2007, Enhancing linear features in image data using horizontal orthogonal gradient ratios: *Computers and Geosciences*, **33**, 981–984, doi: [10.1016/j.cageo.2006.12.002](https://doi.org/10.1016/j.cageo.2006.12.002).
- Dong, G. G., and G. Y. Kuang, 2015, Target recognition in SAR images via classification on Riemannian manifolds: *IEEE Geoscience and Remote Sensing Letters*, **12**, 199–203, doi: [10.1109/LGRS.2014.2332076](https://doi.org/10.1109/LGRS.2014.2332076).
- Fedi, M., and G. Florio, 2001, Detection of potential fields source boundaries by enhanced horizontal derivative method: *Geophysical Prospecting*, **49**, 40–58, doi: [10.1046/j.1365-2478.2001.00235.x](https://doi.org/10.1046/j.1365-2478.2001.00235.x).
- Felsberg, M., and G. Sommer, 2001, The monogenic signal: *IEEE Transactions on Signal Processing*, **49**, 3136–3144, doi: [10.1109/78.969520](https://doi.org/10.1109/78.969520).
- Felsberg, M., and G. Sommer, 2004, The monogenic scale-space: A unifying approach to phase-based image processing in scale-space: *Journal of*

- Mathematical Imaging and Vision, **21**, 5–26, doi: [10.1023/B:JMIV.0000026554.79537.35](https://doi.org/10.1023/B:JMIV.0000026554.79537.35).
- Grauch, V. J. S., and L. Cordell, 1987, Limitations of determining density or magnetic boundaries from the horizontal gradient of gravity or pseudo gravity data: *Geophysics*, **52**, 118–121, doi: [10.1190/1.1442236](https://doi.org/10.1190/1.1442236).
- Hansen, R. O., and E. deRidder, 2006, Linear feature analysis for aeromagnetic data: *Geophysics*, **71**, no. 6, L61–L67, doi: [10.1190/1.2357831](https://doi.org/10.1190/1.2357831).
- Hassan, H. H., and S. V. R. Yalamanchili, 2013, Monogenic signal decomposition: A new approach to enhance magnetic data: 83rd Annual International Meeting, SEG, Expanded Abstracts, 1206–1210.
- Hsu, S. K., J. C. Sibuet, and C. T. Shyu, 1996, High-resolution detection of geologic boundaries from potential-field anomalies: An enhanced analytic signal technique: *Geophysics*, **61**, 373–386, doi: [10.1190/1.1443966](https://doi.org/10.1190/1.1443966).
- Miller, H. G., and V. Singh, 1994, Potential field tilt — A new concept for location of potential field sources: *Journal of Applied Geophysics*, **32**, 213–217, doi: [10.1016/0926-9851\(94\)90022-1](https://doi.org/10.1016/0926-9851(94)90022-1).
- Nabighian, M. N., 1972, The analytical signal of 2D magnetic bodies with polygonal cross-section: Its properties and use for automated anomaly interpretation: *Geophysics*, **37**, 507–517, doi: [10.1190/1.1440276](https://doi.org/10.1190/1.1440276).
- Nabighian, M. N., 1984, Toward a three-dimensional automatic interpretation of potential field data via generalized Hilbert transforms: Fundamental relations: *Geophysics*, **49**, 780–786, doi: [10.1190/1.1441706](https://doi.org/10.1190/1.1441706).
- Nabighian, M. N., V. J. S. Grauch, R. O. Hansen, T. R. LaFehr, Y. Li, J. W. Peirce, J. D. Phillips, and M. E. Ruder, 2005, The historical development of the magnetic method in exploration: *Geophysics*, **70**, no. 6, 33ND–61ND, doi: [10.1190/1.2133784](https://doi.org/10.1190/1.2133784).
- Roest, W. R., J. Verhoef, and M. Pilkington, 1992, Magnetic interpretation using the 3-D analytic signal: *Geophysics*, **57**, 116–125, doi: [10.1190/1.1443174](https://doi.org/10.1190/1.1443174).
- Santos, D. F., J. B. C. Silva, V. C. F. Barbosa, and L. F. S. Braga, 2012, Deep-pass — An aeromagnetic data filter to enhance deep features in marginal basins: *Geophysics*, **77**, no. 3, J15–J22, doi: [10.1190/geo2011-0146.1](https://doi.org/10.1190/geo2011-0146.1).
- Thurston, J. B., and R. S. Smith, 1997, Automated conversion of magnetic data to depth, dip and susceptibility contrast using the SPI(TM) method: *Geophysics*, **62**, 807–813, doi: [10.1190/1.1444190](https://doi.org/10.1190/1.1444190).
- Uieda, L., V. C. Oliveira, Jr, and V. C. F. Barbosa, 2013, Modeling the earth with Fatiando a Terra: Techniques: Presented at 12th Python in Science Conference, SCIPY 2013, 90–96.
- Verduzco, B., J. D. Fairhead, C. M. Green, and C. MacKenzie, 2004, New insights to magnetic derivatives for structural mapping: *The Leading Edge*, **23**, 116–119, doi: [10.1190/1.1651454](https://doi.org/10.1190/1.1651454).
- Wijns, C., C. Perez, and P. Kowalczyk, 2005, Theta map: Edge detection in magnetic data: *Geophysics*, **70**, no. 4, L39–L43, doi: [10.1190/1.1988184](https://doi.org/10.1190/1.1988184).
- Zalán, P. V., 2011, Fault-related folding in the deep waters of the equatorial margin of Brazil, in K. McClay, J. H. Shaw, and J. Suppe, eds., Thrust fault-related folding: AAPG Memoir 94, 335–355.
- Zhang, H. L., D. Ravat, Y. R. Marangoni, and X. Y. Hu, 2014, NAV-Edge: Edge detection of potential-field sources using normalized anisotropy variance: *Geophysics*, **79**, no. 3, J43–J53, doi: [10.1190/geo2013-0218.1](https://doi.org/10.1190/geo2013-0218.1).